Unified description of hadron yield ratios from dynamical core-corona initialization

Yuuka Kanakubo, Yasuki Tachibana, and Tetsufumi Hirano

Phys. Rev. C **101**, 024912 — Published 24 February 2020

DOI: 10.1103/PhysRevC.101.024912

Unified description of hadron yield ratios from dynamical core–corona initialization

Yuuka Kanakubo,[1,*] Yasuki Tachibana,[2,1,†] and Tetsufumi Hirano[1,‡]

[1] *Department of Physics, Sophia University, Tokyo 102-8554, Japan*
[2] *Department of Physics and Astronomy, Wayne State University, Detroit, MI 48201, USA*

(Dated: January 29, 2020)

We develop the dynamical core–corona initialization framework as a phenomenological description of the quark gluon plasma (QGP) fluids formation in high-energy nuclear collisions. Using this framework, we investigate the fraction of the fluidized energy to the total energy and strange hadron yield ratios as functions of multiplicity and scrutinize the multiplicity scaling of hadron yield ratios recently reported by ALICE Collaboration. Our results strongly indicate that the QGP fluids are partly formed even at the averaged multiplicity for non-single diffractive p+p events.

PACS numbers: 25.75.-q, 12.38.Mh, 25.75.Ld, 24.10.Nz

I. INTRODUCTION

Properties of the quark gluon plasma (QGP) have been investigated through high-energy nuclear collision experiments at the Relativistic Heavy Ion Collider (RHIC) at Brookhaven National Laboratory and at the Large Hadron Collider (LHC) at CERN. The experimental results have brought us a great deal of information about properties of the QGP. The collective behavior of the QGP is well described by relativistic hydrodynamics [1–5] in which the system is postulated to keep local thermal equilibrium during expansion. Since dissipative effects on expansion are quite small regardless of remarkably large expansion rate, the QGP exhibits near-perfect fluidity, which has led to the concept of strongly coupled/interacting QGP (sQGP) [2–4].

Comparisons of the experimental results from heavy-ion collisions with those from small colliding systems, such as proton-proton and proton-nucleus collisions, have been made to see how small the QGP droplets can be. Small colliding systems had been believed to provide us with reference data for a long time since the size of the matter is too small to reach local thermal equilibrium. However, recent experimental data imply the QGP formation even in small colliding systems (for reviews, see, *e.g.*, Refs. [6, 7]). One of those data shows sizable azimuthal anisotropy in final hadron distributions [8–14], which can be interpreted as a result of the hydrodynamic response of the QGP medium to the initial collision geometry [15–22]. Although this has been discussed actively from relativistic hydrodynamics, another interpretation is brought about also by the color glass condensate picture, which gives long-range correlation in rapidity in small colliding systems without invoking the QGP formation [23–36]. Thus the origin of collectivity observed in small colliding system still remains to be understood.

Besides the azimuthal anisotropy, the strangeness enhancement in small colliding systems is reported by ALICE Collaboration [37]. Yield ratios of (multi-)strange hadrons to charged pions are measured and exhibit monotonic and continuous increase as functions of multiplicity. Even in small colliding systems, the strange hadron yield ratios in high-multiplicity events almost reach the values in heavy-ion collisions.

Strangeness enhancement was proposed to be a signal of the QGP formation in high-energy nuclear collisions a long time ago [38, 39]. Since initial colliding nuclei do not contain the strange quark as valence one, yields of strange hadrons would be sensitive to details of reaction dynamics. If the production rate of strange quarks becomes sufficiently high in thermalized systems, chemical equilibrium of strange quarks besides up and down quarks is expected to be reached within the time scale of nuclear collisions. In fact, most of the yield ratios of hadrons including multi-strange baryons have been well reproduced by statistical models [40], which is recognized to be one of the strong signals of the QGP formation in heavy-ion collisions at RHIC and the LHC energies. Therefore the strangeness enhancement in high-multiplicity proton-proton and proton-nucleus collisions reported by ALICE Collaboration [37] strongly indicates the QGP formation even in such a small colliding system.

This continuous increase of the strange hadron yield ratio can be interpreted as follows. Final hadrons originate from two different sources having different hadron production processes. The values of yield ratios in low-multiplicity events are described by results from the string fragmentation, in which the string tension ($\kappa \approx 1$ GeV/fm) controls the yield ratios of hadrons. On the other hand, the values of yield ratios in high-multiplicity events are explained by the statistical hadronization approach where the matter is assumed to be in chemical equilibrium. In this case, chemical freezeout temperature ($T_{\rm ch} \approx 160$ MeV) plays an essential role in describing yield ratios of hadrons. Thus, the dominant process of final hadron production is supposed to change gradually from string fragmentation at low-multiplicity limit to

* y-kanakubo-75t@eagle.sophia.ac.jp
† yasuki.tachibana@wayne.edu
‡ hirano@sophia.ac.jp

statistical hadronization at high-multiplicity limit. In the intermediate multiplicity, final hadron production would be superposition of these two contributions.

The "core–corona" picture has been adopted to demonstrate the above idea [41–46]. At the first contact of two nuclei, the number of collisions per nucleon should be different depending on where they are located in the transverse plane being perpendicular to the collision axis. High-density regions just after the initial collision in which nucleons in colliding nuclei suffer a lot of collisions are called "core" and assumed to be sources of the QGP medium in local thermal and chemical equilibrium. Low-density regions in which nucleons suffer only a few collisions are referred to as "corona" and supposed to be likely to create hadrons via string fragmentation without formation of bulk medium. Since the "core" regions become dominant production mechanism with increasing multiplicity, the continuous change from string fragmentation to statistical hadronization with increasing multiplicity could naturally be explained by the "core–corona" picture.

In this paper, we introduce the core–corona picture into the dynamical initialization framework to obtain the unified description of hadron yield ratios from small colliding systems to heavy-ion collisions. The dynamical initialization framework [47–50] describes the dynamics of gradual forming of the QGP fluids phenomenologically.[1] Under this framework, the initial condition of the QGP fluids is obtained via energy-momentum deposition from the partons/strings/fields generated just after the collision. As extension of the dynamical initialization description for QGP fluids generation from initially produced partons [47–50], we introduced the dependence on initial parton densities in the dynamical initialization [50], which we call the "dynamical core–corona initialization (DCCI) model" in this paper. Given the various definitions of the core and the corona in the literature [41–46], we here define them explicitly as follows: The core represents the fluids under local thermal and chemical equilibrium, while the corona represents the system composed of non-equilibrated partons traversing the fluids or the vacuum. In the DCCI model, the continuous separation between the core and the corona is attributed to the spatial density of initially produced partons. Thus, it should be emphasized that we do not introduce the threshold to separate the core from the corona explicitly unlike the model in Refs. [45, 46]. In the DCCI model, the non-equilibrated partons can coexist with the fluids at some space-time point.

This paper is organized as follows: In Sec. II, we give an overview of the dynamical initialization framework and its extension to the DCCI model. In Sec. III, we first investigate how much the energy is fluidized at midrapidity when we reproduce the multiplicity dependence of particle ratio from experimental data using the DCCI model. Then we extract the fraction of fluidized energy as a function of multiplicity from experimental data in both small and large colliding systems at LHC energies. After that we discuss a universal behavior of the hadron yield ratios as functions of multiplicity. Finally Section IV is devoted to summary of this paper.

Throughout this paper, we use the natural unit, $\hbar = c = k_B = 1$, and the Minkowski metric, $g_{\mu\nu} = \mathrm{diag}(1, -1, -1, -1)$.

[1] The dynamical initialization framework is essential in description of nuclear collisions at lower energies since hadrons are gradually generated due to insufficient Lorentz-contraction of the colliding nuclei [48, 49].

II. MODEL

Before going into detailed explanations, we briefly give an outline of the DCCI model employed in this paper. Initial partons are obtained with the Monte Carlo event generator PYTHIA [51] and start traveling in the vacuum at their formation time. QGP fluids are dynamically generated via energy-momentum deposition from these partons by solving the relativistic hydrodynamic equation with source terms. Here the four-momentum deposition per unit time is parametrized to be proportional to the initially produced parton density so that we take into account the core–corona picture: Partons in regions with larger density of surrounding partons are more likely to deposit their four-momentum and generate QGP fluids, while those in dilute regions tend to traverse keeping their four-momentum that they have just after the collision of nuclei. In this way, separation of initially produced partons into the QGP fluids (the core) and the non-equilibrated partons (the corona) is settled as a consequence of dynamical four momentum deposition of each parton. After the dynamical initialization with the core–corona picture, we continue hydrodynamic evolution for fluids until their temperature drops to the decoupling temperature. Fluids are particlized into the hadrons at the decoupling hypersurface via the Cooper–Frye formula [52]. On the other hand, surviving partons are hadronized under the string fragmentation in PYTHIA. Therefore, the final hadron yield in this model is a summation of the contribution from particlization of the medium under local thermal and chemical equilibrium and that from string fragmentation.

A. Hydrodynamic equations with source terms

In conventional hydrodynamic simulations, the equation of continuity for energy and momentum,

$$\partial_\mu T^{\mu\nu}(x) = 0, \tag{1}$$

is solved, where $T^{\mu\nu}$ is the energy-momentum tensor of the fluid assuming that the energy-momentum conservation is satisfied within the fluid. However, during the

formation of the locally equilibrated medium in high-energy nuclear collisions, there exist incoming energy and momentum for the formation of the medium from non-equilibrated subsystems. In our DCCI model, the initially produced partons deposit their energy and momentum for the formation of the medium fluid and the energy-momentum conservation is imposed for the total system which is a composite one of the medium fluids and the traversing partons,

$$\partial_\mu T^{\mu\nu}_{\rm tot}(x) = \partial_\mu \left(T^{\mu\nu}_{\rm fluid}(x) + T^{\mu\nu}_{\rm parton}(x) \right) = 0. \quad (2)$$

Here we assume that energy and momentum deposited by partons are equilibrated instantaneously. Equation (2) can be written in the form of the relativistic hydrodynamic equation with source term,

$$\partial_\mu T^{\mu\nu}_{\rm fluid}(x) = J^\nu(x)\,, \quad (3)$$

if the source term is defined as

$$J^\nu = -\partial_\mu T^{\mu\nu}_{\rm parton}. \quad (4)$$

The hydrodynamic equation with source term (3) is also commonly used in the simulations to discuss the physics of jet quenching and its effects on the medium responses [53–58]. If we assume ideal fluids, the energy-momentum tensor of QGP fluids is decomposed as

$$T^{\mu\nu}_{\rm fluid} = (e+P)u^\mu u^\nu - P g^{\mu\nu}. \quad (5)$$

Here, e, P, and u^μ are energy density, hydrostatic pressure, and velocity of the fluid, respectively. In order to close the equations of motion, we need the equation of state (EoS) which has a form of hydrostatic pressure as a function of energy density, $P = P(e)$. In this study, we adopt the EoS from (2+1) flavors lattice QCD calculations [59]. In other words, u, d, and s quarks (and their anti-quarks) and gluons are under thermal and chemical equilibrium in the QGP fluids.

In this study, we do not solve the equation for the conservation of charges, such as baryon number, strangeness and electric charges, since matters generated at RHIC and the LHC energies are supposed to be almost baryon-free, strangeness-neutral, and charge-neutral around the midrapidity.

We also note that, although Eqs. (3) and (5) are denoted in Cartesian coordinates to avoid complex notations, the actual calculation is performed in Milne coordinates. In Milne coordinates, the time axis is represented with proper time $\tau = \sqrt{t^2 - z^2}$. The other spatial coordinates are x and y which are the transverse coordinates being perpendicular to the collision axis, and $\eta_s = (1/2)\ln[(t+z)/(t-z)]$ which is space-time rapidity.

B. Dynamical initialization of QGP fluids

In this study, the phase space distribution of initially produced partons is assumed to be

$$f_{\rm parton}(\boldsymbol{x},\boldsymbol{p};t) d^3x d^3p = \sum_i G(\boldsymbol{x}-\boldsymbol{x}_i(t)) \delta^{(3)}(\boldsymbol{p}-\boldsymbol{p}_i(t)) d^3x d^3p, \quad (6)$$

$$G(\boldsymbol{x}-\boldsymbol{x}_i(t))d^3x = \frac{1}{\sqrt{(2\pi\sigma^2)^3}} e^{-\frac{(\boldsymbol{x}-\boldsymbol{x}_i(t))^2}{2\sigma^2}} d^3x. \quad (7)$$

Here σ is a width of Gaussian function in coordinate space. The Gaussian is introduced to give the scale of the region which is supposed to be involved in the interaction by a parton in the model. The trajectory of a parton is assumed to be eikonal and rapidity of a parton is constant during the dynamical initialization, *i.e.*, $y_i = \eta_{s,i} =$ constant where index i represents the i-th parton. Under this assumption, the position of the i-th parton is defined as

$$\boldsymbol{x}_i(t) = \frac{\boldsymbol{p}_i}{p_i^0}(t - t_{{\rm form},i}) + \boldsymbol{x}_{{\rm ini},i}, \quad (8)$$

where $(p_i^0, \boldsymbol{p}_i)$ is the four-momentum of the i-th parton. Here, $\boldsymbol{x}_{{\rm ini},i}$ is the position at the formation time of the i-th parton, $t_{{\rm form},i}$. Under these assumptions, we derive the explicit form of Eq. (4). By putting the phase space distribution in Eq. (6) into the kinetic definition of the energy-momentum tensor, the source term (4) becomes

$$\begin{aligned} J^\mu(x) &= -\partial_\mu T^{\mu\nu}_{\rm parton} \\ &= -\sum_i \int d^3p \frac{p^\mu p^\nu}{p^0} \partial_\mu f_{\rm parton}(\boldsymbol{x},\boldsymbol{p};t) \\ &= -\sum_i \frac{dp_i^\mu(t)}{dt} G(\boldsymbol{x}-\boldsymbol{x}_i(t))\,. \end{aligned} \quad (9)$$

For the detail of this derivation, see Appendix A.

We call dp_i^μ/dt in Eq. (9) the "fluidization rate" which is the rate of four-momentum deposition for the i-th parton. Since the index i represents each parton produced in each event, the summation is taken for all the initial partons in an event.

We assume that QGP fluids are generated by the initial partons during the proper time period from the formation time $\tau = \tau_{00} (= 0.1$ fm) to initial time of fluids $\tau = \tau_0 (= 0.6$ fm). In this paper, the common constant value of τ_{00} is assumed for all partons, $\tau_{{\rm form},i} = \sqrt{t_{{\rm form},i}^2 - z_{{\rm form},i}^2} \equiv \tau_{00}$. We start with the vanishing energy-momentum tensor of QGP fluids, $T^{\mu\nu}_{\rm fluid}(\tau = \tau_{00}) = 0$, and solve Eq. (3) from $\tau = \tau_{00}$ to $\tau = \tau_0$. Here we note that the energy-momentum conservation is satisfied among the QGP fluids and the traversing partons through the dynamical initialization.

As we mentioned in the previous subsection, our actual simulations are performed in the (3+1)-dimensional

Milne coordinates. Thus the explicit form of the Gaussian distribution function in Eq. (9) is replaced as

$$
\begin{aligned}
& G\left(\boldsymbol{x}-\boldsymbol{x}_i(t)\right) d^3x \\
\rightarrow & \frac{1}{2\pi\sigma_\perp^2} \exp\left[-\frac{\left(\boldsymbol{x}_\perp-\boldsymbol{x}_{\perp,i}(\tau)\right)^2}{2\sigma_\perp^2}\right] \\
\times & \frac{1}{\sqrt{2\pi\tau^2\sigma_{\eta_s}^2}} \exp\left[-\frac{\left(\eta_s-\eta_{s,i}(\tau)\right)^2}{2\sigma_{\eta_s}^2}\right] \tau d\eta_s d^2x_\perp, \quad (10)
\end{aligned}
$$

where $\boldsymbol{x}_{\perp,i}(\tau)$ and $\eta_{s,i}(\tau)$ is the transverse coordinates and the space-time rapidity of the i-th parton. In this study, we adopt $\sigma_\perp = 0.5$ fm and $\sigma_{\eta_s} = 0.5$ for transverse and longitudinal widths of Gaussian function, respectively.

C. Energy-momentum deposition rate with the core–corona picture

We introduce the core–corona picture as an extension of the dynamical initialization framework [50]. To introduce the core–corona picture, we parametrize the fluidization rate as

$$
\frac{dp_i^\mu}{dt}(t) = -a_0 \frac{\rho_i(\boldsymbol{x}_i(t))}{{p_{T,i}}^2} p_i^\mu(t), \quad (11)
$$

where $p_{T,i}$ and p_i^μ are the transverse momentum and the four-momentum of the i-th parton, respectively. Here, ρ_i is the spatial density of partons surrounding the i-th parton. It is defined as

$$
\begin{aligned}
\rho_i(\boldsymbol{x}_i(t)) d^3x &= \rho_i(\boldsymbol{x}=\boldsymbol{x}_i(t)) d^3x \\
&= \sum_{j\neq i} G\left(\boldsymbol{x}-\boldsymbol{x}_j(t)\right) d^3x\big|_{\boldsymbol{x}=\boldsymbol{x}_i(t)}. \quad (12)
\end{aligned}
$$

The dimensionless factor a_0 is a free parameter to control the intensity of energy-momentum deposition. The Gaussian function G has the same form as the one introduced in Eq. (6) with the form of Eq. (10) in Milne coordinates.

The parton density ρ_i introduced in Eq. (11) is the key factor to capture the feature of the core–corona picture. In high parton density regions, a large fraction of the energy and momentum of the parton is deposited to create the QGP fluids through the source term in Eq. (3). On the other hand, fluids are not likely to be generated in low parton density regions. It should be emphasized here that the criteria for the formation of the medium fluid is not governed by a certain threshold for the parton density but by the configuration of initial partons and their dynamics. In this framework, medium fluids and non-equilibrated partons can even coexist at the same space-time point.

The factor ${p_T}^{-2}$ in the fluidization rate accounts for the tendency that lower p_T partons are more likely to deposit their energy and momentum to form the fluids. We should note that the power of -2 comes from consideration of dimension in Eq. (11). Although one may use more complicated forms of the fluidization rate to capture the equilibration processes, we leave this consideration for our future work.

As we discuss in the next subsection, the event generator Pythia, which we employ for generation of initial partons, provides us with the color flows of partons to form strings. During the dynamical core–corona initialization, we trace color flows of the partons in every time step and calculate the invariant mass of each string. As the partons lose their energy and momentum, the invariant mass of strings becomes smaller and, eventually, some strings cannot be performed string fragmentation due to the lack of their invariant masses. To avoid such a situation, we assign the threshold of invariant mass for each string. If the invariant mass becomes below the threshold to undergo the string fragmentation in Pythia, we put all the energy and momentum of partons in that string into fluids. In this paper, we use the threshold of invariant mass as $m_{\rm th} = m_1 + m_2 + 1.0$ in the unit of GeV for strings which have quark/anti-diquark and anti-quark/diquark at the each end point. Here m_1 and m_2 are the constituent masses of leading quark/anti-diquark and anti-quark/diquark.

D. Generation of initial partons

In our DCCI framework, the event generator Pythia 8.230 [51] is used to simulate the initial parton production. In Pythia, we switch on the option to obtain partonic vertices (`PartonVertex:setVertex=on`) and switch off the hadronization (`HadronLevel:all=off`) to obtain the phase space distribution of partons at $\tau = \tau_{00}$. Pythia provides us with the vertices for parton production through multi parton interactions, final state radiations, and initial state radiations [60] which can be used in Eq. (8). Since the Milne coordinates are employed in the actual simulations, we take the transverse coordinates of the i-th parton, $\boldsymbol{x}_{\perp{\rm ini},i}$, directly from Pythia and assume $\eta_{s{\rm ini},i} = y_{{\rm ini},i}$, where $y_{{\rm ini},i}$ is rapidity of a parton generated with Pythia. Here, it should be noted that this version of Pythia handles heavy-ion reactions at high-energies using the Angantyr model [61, 62].

E. Particlization of QGP fluids

The dynamics of medium after $\tau = \tau_0$ is treated in the same way as that in conventional hydrodynamic simulations. In this paper, we do not consider the energy and momentum loss of traversing partons due to the parton-medium interaction after $\tau = \tau_0$ for simplicity and solve Eq. (3) without the source term until the maximum temperature of fluids becomes lower than the fixed decoupling temperature $T_{\rm dec} = 160$ MeV. The effects of

medium response on anisotropic flow in the dynamical initialization can be found in Ref. [47].

We use the Cooper–Frye formula [52] to obtain spectra of hadrons emitted directly from the decoupling hypersurface. The yields from the medium fluids are obtained by integrating the spectra of each hadron species i

$$N_i = \frac{g_i}{(2\pi)^3}\int \frac{d^3p}{p^0}\int_\Sigma \frac{p^\mu d\sigma_\mu(x)}{\exp\left[p^\mu u_\mu(x)/T_{\rm dec}\right] \mp_{\rm BF} 1}, \quad (13)$$

where g_i is the degeneracy, $\mp_{\rm BF}$ corresponds to Bose or Fermi distributions, Σ is the decoupling hypersurface at $T = T_{\rm dec}$, and $d\sigma_\mu$ is the normal vector of its hypersurface. Since we assume baryon-free matter in this paper, the chemical potential of baryon number does not appear in Eq. (13). Here we should note that some fluid elements are already lower than the decoupling temperature at $\tau = \tau_0$. For such fluid elements, we assume that the particlization is performed at the initial time of fluid $\tau = \tau_0$ with the corresponding temperature.

For the consideration of feed down from resonance decays, we correct the direct yields based on statistical model calculations [40]. We estimate the ratio of the total yields to the contribution from directly produced hadrons c_i from Fig. 2 of Ref. [40], and multiply the ratio c_i with the direct yield obtained from Eq. (13). Here we use the ratio factors, $c_\pi = 3.2$, $c_p = 3.0$, $c_\Lambda = 4.7$, $c_\Xi = 1.7$, and $c_\phi = 1.0$, to obtain the total yields of these hadrons.

F. String fragmentation of traversing partons

We assume that the partons surviving after the dynamical core–corona initialization form color singlet strings and are hadronized under the string fragmentation. We push back the surviving partons into Pythia with their energy and momentum at $\tau = \tau_0$ (note that no parton energy loss happens after $\tau = \tau_0$ in this paper) and perform hadronization with the option `forceHadronLevel()` to get the final hadronic spectra. Here we correct the energy of parton to be mass-on-shell using the momentum at $\tau = \tau_0$ and rest-mass for the execution of the string fragmentation, since most partons are mass-off-shell due to the four-momentum deposition of Eq. (11). We checked that the violation of energy conservation due to this correction is small enough to be ignored. It should also be noted that we switch off weak decays of strange baryons which are stable against strong decays (except $\Sigma^0 \to \Lambda + \gamma$) in Pythia .

III. RESULTS

The parton density distribution ρ_i in the fluidization rate per parton (11) governs the separation of the core and the corona. In the dynamical core–corona initialization, partons traversing high-density region tend to deposit their four-momentum and to generate the fluids (the core). In contrast, partons traversing low-density region tend to stay as surviving partons (the corona). As a result of the dynamical core–corona initialization, the final hadron yields contain the contributions from those two components. The fraction of each contribution is sensitive to distribution of the parton density from event to event.

In the following, the multiplicity $\langle dN_{\rm ch}/d\eta\rangle$ describes the number of charged particles per unit pseudorapidity in $|\eta| < 0.5$ calculated with default settings in Pythia. To obtain the hadron yield ratios, we first calculate final hadron yields from the core and the corona separately and the final hadron yield in each multiplicity class is the sum of them,

$$\left\langle \frac{dN_i}{dy} \right\rangle = \left\langle \frac{dN_i}{dy} \right\rangle_{\rm core} + \left\langle \frac{dN_i}{dy} \right\rangle_{\rm corona}. \quad (14)$$

The angle bracket means the event average in a multiplicity class. Although the final yield should be obtained as a sum of two contributions from the core and the corona on an event-by-event basis, the number of events for hydrodynamic simulations is smaller than that for parton generation and hadronization in Pythia in order to reduce the computational cost. In the results of the hadron yield ratios, error bars represent statistical ones of yields from string fragmentation in Pythia, while the shaded band represents statistical errors from the number of events in hydrodynamic simulations. Since central collisions are more weighted and the corresponding weight factor is provided for each event in the heavy-ion mode in Pythia, we consider it in our statistical analysis. We also note that the hadron yields from the core are calculated via the Eq. (13) at $y = 0$ assuming approximate boost invariance. On the other hand, the hadron yields from the corona are obtained by counting the hadrons in $|y| < 2.0$ to gain sufficient statistics.

A. Parameter a_0 dependence on particle ratio

The free parameter a_0 in Eq. (11) controls intensity of the fluidization of partons besides the ρ_i. First we check the a_0 dependence on the particle ratio. We perform simulations of Pb+Pb collisions at $\sqrt{s_{NN}} = 2.76$ TeV with $a_0 = 10, 20$, and 100 in the DCCI model.

Figure 1 shows the hadron yield ratio of cascades $(\Xi^- + \bar{\Xi}^+)$ to charged pions $(\pi^+ + \pi^-)$ as a function of multiplicity, *i.e.*, the event-averaged charged hadron pseudo-rapidity density $\langle dN_{\rm ch}/d\eta\rangle$ at mid-rapidity $|\eta| < 0.5$. [2] The hadron yield ratios in Pb+Pb collisions at

[2] It should be noted that it is better to see the increasing behaviour of the yield ratio of omega baryons since it shows more rapid enhancement. However, we do not calculate them since it is statistically difficult to obtain enough yield of omega baryons within our framework.

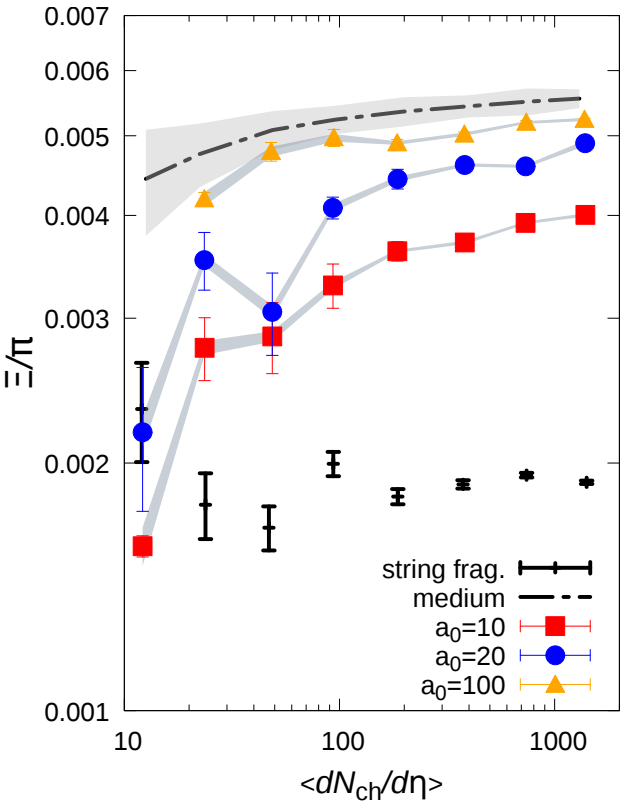

FIG. 1. (Color Online) Parameter a_0 dependence on hadron yield ratios of cascades to charged pions as functions of multiplicity in Pb+Pb collisions at $\sqrt{s_{NN}} = 2.76$ TeV. Results of $a_0 = 10$ (squares), 20 (circles), and 100 (triangles) are shown for comparison. The error bars of the hadron yield ratio are originated from the statistical errors of hadron yields from string fragmentations with PYTHIA, while the shaded band comes from the statistical errors of yields from hydrodynamic simulations. The hadron yield ratios only from the medium or string fragmentation are also shown as references.

$\sqrt{s_{NN}} = 2.76$ TeV with three different a_0 parameters are shown as closed symbols. We also show results with two limited cases: One with the case that all partons are fluidized and the other with default setting in heavy-ion mode in PYTHIA, which are referred as "medium" and "string frag." in Fig. 1.

As an overall tendency, the hadron yield ratio monotonically increases with multiplicity and saturates in high-multiplicity events. More specifically, results with $a_0 = 10$ and 20 reflect the value from the corona $N_\Xi/N_\pi \approx 0.002$ at low-multiplicity and saturates towards the one from the core $N_\Xi/N_\pi \approx 0.005$ at high-multiplicity. This is because the dominant contribution for the final yields changes from the corona to the core as multiplicity increases. In addition to this, the hadron yield ratio with larger a_0 tends to saturate at smaller multiplicity. It can be naturally expected from a fact that the parameter a_0 controls the amount of four-momentum deposition from initial partons from Eq. (11). The results shown in Fig. 1 demonstrate this expectation.

We also note that the hadron yield ratios from both the fluids and the string fragmentation do not seem to depend much on the multiplicity since the hadron yield ratios from the core are determined from the decoupling temperature $T_{\rm dec}$ while the ones from the corona are determined from the string tension κ.

To make a more quantitative discussion on how the parameter a_0 affects the hadron yield ratio as a function of multiplicity, we fit the results shown in Fig. 1 by the function

$$f(x) = (F - S)\frac{x^n}{x^n + k^n} + S, \tag{15}$$

where the valuable x denotes multiplicity. Here we use $F = 0.0055$ and $S = 0.0018$ for the hadron yield ratio of cascades to charged pions purely from fluids and that from string fragmentation, respectively, assuming that the ratio from those components is constant as a function of multiplicity.[3] The function in Eq. (15) captures the behavior of the multiplicity dependence of hadron yield ratios,

$$\lim_{x\to\infty} f(x) = F, \quad \lim_{x\to 0+} f(x) = S. \tag{16}$$

This fitting function has two fitting parameters, k and n. Using this function, we quantify the multiplicity, $x_{\rm sat}$, at which the hadron yield ratio reaches 90 % of the difference between the values obtained from the fluids and the one from string fragmentation, namely, $f(x_{\rm sat}) = S + 0.9(F - S)$. Once the results are fitted, $x_{\rm sat} = k\sqrt[n]{9.0}$, which is referred as saturation multiplicity, is obtained. For details of the fittings, see Appendix B.

Figure 2 shows the a_0 dependence of saturation multiplicity. As it can be expected from results shown in Fig. 1, the saturation multiplicity exhibits a clear monotonic decrease as a function of a_0. We also simulate p+p collisions at $\sqrt{s} = 7$ TeV and p+Pb collisions at $\sqrt{s_{NN}} = 5.02$ TeV in addition to Pb+Pb collisions with $a_0 = 100$ in the DCCI model and perform the function fittings of these results simultaneously. Even if we include results from p+p and p+Pb collisions in the fitting, the resultant saturation multiplicity is almost identical with the one only from Pb+Pb collisions with the same a_0 value. We also apply the global fitting for the ALICE experimental data in p+p, p+Pb, and Pb+Pb collisions [37, 64, 65] and estimate its saturation multiplicity as $\langle dN_{\rm ch}/d\eta\rangle \approx 31$ shown as a solid line.

The value of the parameter a_0 which is most likely to reproduce the experimental data can be extracted by fitting the results obtained in the DCCI model in Fig. 2.

[3] This function is motivated by Hill equation which characterizes ligand bindings in biochemical reaction [63].

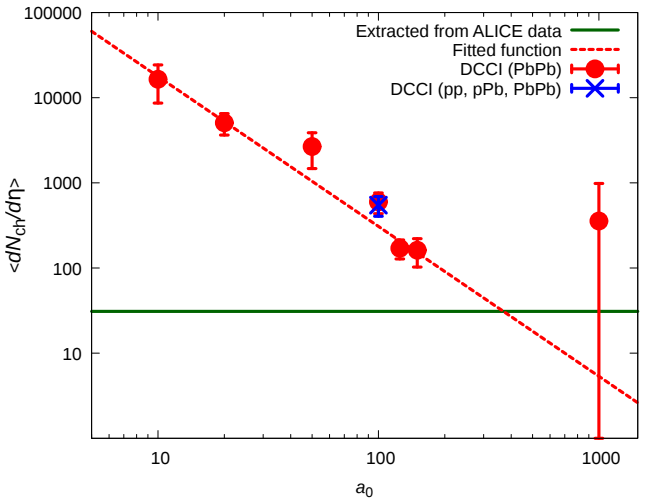

FIG. 2. (Color Online) Parameter a_0 dependence of saturation multiplicity in Pb+Pb collisions (circles) are compared with the result from simultaneous fitting for p+p, p+Pb and Pb+Pb collisions (cross) and that from fitting for the experimental data (horizontal line). Dashed line shows the fitting function for the saturation multiplicities (circles) fitted by using a power function.

Regarding the a_0 dependence of saturation multiplicity as a power function, we obtain the optimized function, $f(a_0) = a_0^{-1.8} \times 10^6$, with reduced chi-square $\chi^2 \approx 1.2$. This optimized function is shown as a dashed line in Fig. 2. The value of a_0 at the intersection point of the solid and dashed lines in Fig. 2 brings us to reproduce the experimental data most reasonably within the DCCI model. We estimate this value to be $a_0 \approx 368$. Here, to obtain the optimized value for a_0, we use the central value of the plots from fitting for the experimental data in Fig. 2.

B. Fraction of the fluidized energy

We simulate p+p, p+Pb, and Pb+Pb collisions with $a_0 = 368$ in the DCCI model to demonstrate how much energy and momentum just after the collisions are turned into the fluids. We define the fraction of fluidized energy as

$$R = \left. \frac{dE_{\rm fluid}/d\eta_s}{dE_{\rm tot}/d\eta_s} \right|_{\eta_s=0}. \quad (17)$$

which is the ratio of the energy density turned into the fluids to the total energy density at midrapidity ($\eta_s = 0$). The fluidized energy can be obtained by integrating the time component of source terms from $\tau = \tau_{00}$ (formation time) to $\tau = \tau_0$ (hydrodynamic initial time) in the transverse plane as

$$\left. \frac{dE_{\rm fluid}}{d\eta_s} \right|_{\eta_s=0} = \int_{\tau_{00}}^{\tau_0} d\tau \int d^2x_\perp \tau J^\tau(\tau, x_\perp, \eta_s = 0). \quad (18)$$

The total energy density $dE_{\rm tot}/d\eta_s$ is calculated by taking the sum of all the initial partons' energy at $\tau = \tau_{00}$.

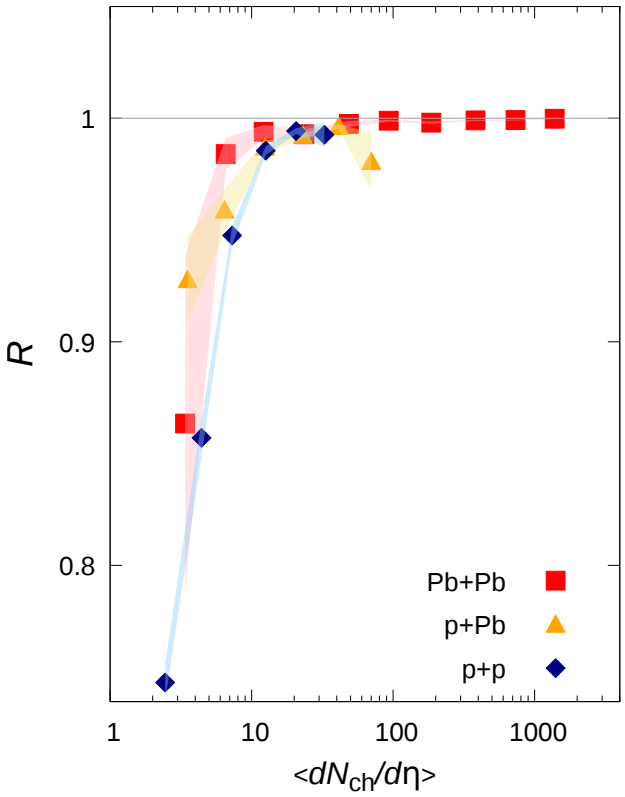

FIG. 3. (Color online) Fraction of the fluidized energy to the total energy at $\eta_s = 0$ as a function of multiplicity at midrapidity, $\langle dN_{\rm ch}/d\eta \rangle$ ($|\eta| < 0.5$), in p+p (diamonds) collisions at $\sqrt{s} = 7$ TeV, p+Pb (triangles) collisions at $\sqrt{s_{NN}} = 5.02$ TeV, and Pb+Pb (squares) collisions at $\sqrt{s_{NN}} = 2.76$ TeV.

In Fig. 3, the fraction of fluidized energy R in p+p, p+Pb, and Pb+Pb collisions is shown as a function of multiplicity. The results exhibit the multiplicity scaling regardless of system sizes or collision energies. R increases monotonically and saturates around $\langle dN_{\rm ch}/d\eta \rangle_{|\eta|<0.5} \approx 20$. It is noted that hydrodynamic simulations are performed in the center-of-mass frame while multiplicities are calculated in the laboratory frame. Therefore there is a rapidity shift $\Delta\eta_s = 0.47$ in p+Pb collisions at $\sqrt{s_{NN}} = 5.02$ TeV between those frames. The most remarkable thing is that the fraction of fluidized energy R is finite even at the averaged multiplicity for non-single diffractive p+p events, $\langle dN_{\rm ch}/d\eta \rangle = 5.74 \pm 0.15$ [66], which is generally considered to be too small to generate the QGP. This means

that, within our model calculations, the contribution from the fluids to final hadron yields is crucial to reproduce the yield ratio of cascades to pions in those multiplicity events. Therefore this would be the strong indication of the partial QGP generation even in non-single diffractive p+p collisions at $\sqrt{s} = 7$ TeV.

We should note that the fraction of fluidized energy R could be over-estimated quantitatively in the DCCI model. Suppose some hadronic strings are stretched between two surviving partons (possibly between a quark/anti-quark and a di-quark/anti-di-quark) each of which is in the projectile and in the target regions. Although these strings do not contain partons near midrapidity, they can decay into hadrons in the midrapidity region. We find ≈10% of the yield at midrapidity is originated from these strings even when all partons are fluidized in midrapidity region, *i.e.*, $R \approx 1$. It is expected that such strings would melt when they penetrate the deconfined matter and do not contribute to the final hadron yield at midrapidity. This issue is to be resolved as future work.

C. Hadron yield ratios

We show the various hadron yield ratios in p+p, p+Pb, and Pb+Pb collisions as functions of multiplicity and compare them with ALICE data. In Fig. 4, the yield ratios as functions of multiplicity are shown for (a) cascades with $|S| = 2$, (b) lambdas with $|S| = 1$, (c) phi mesons with $|S| = 0$, and (d) protons and anti-protons. In the DCCI model, we use $a_0 = 368$ extracted in Sec. III A. Since the parameter a_0 is fitted for experimental data of cascades, we reproduce the behavior of them well as shown in Fig. 4(a). In addition, we also reproduce experimental data for lambdas and phi mesons reasonably well. From Fig. 3, it is clear that the continuous change of hadron yield ratios results from competition between contribution between the core and the corona. Thus, continuous change of dominant particle production mechanism from the corona to the core enables the model to describe the experimental data. These results also indicate that the DCCI model describes the different tendency of strangeness enhancement among strange baryons which have different strangeness quantum numbers.

It is noted that the increasing behavior of the phi meson yield ratios would not be described by the canonical suppression model [69] since phi mesons are the hadrons with hidden strangeness. According to the fact that the models based on the core–corona picture including our model show good agreement with the experimental data [46, 50, 72], the core–corona picture turns out to be more essential description of the multiplicity dependence of hadron yield ratios rather than the canonical suppression model.

Regarding proton and anti-proton yield ratios, our results show continuous increase with multiplicity which is the same behavior as the other hadron yield ratios from the DCCI model. However, the experimental data exhibit the opposite tendency: The data decrease with the multiplicity and deviate gradually from our results. The value of the ratio of protons and anti-protons to charged pions from the DCCI model is ≈ 0.05-0.06 in a few lowest-multiplicity bins, which is almost the same value as the one that the corona gives. On the other hand, the ratio is ≈ 0.07 in the highest-multiplicity bin in this model, which is almost consistent with the value obtained from the core. Thus the difference between our results and the experimental data in high-multiplicity events indicate a mechanism missing in the present model. Since this deviation can be explained from baryon anti-baryon annihilation during hadronic evolution [46, 70], we might resolve this issue combining our model with hadronic cascade models in the late stage.

Motivated by a fact that hadron yield ratios scale with multiplicity regardless of system size or collision energy in the ALICE data [37], we study whether the DCCI model gives the same tendency or not. To see the system size independence at the LHC energies, the hadron yield ratios in Xe+Xe collisions at $\sqrt{s_{NN}} = 5.44$ TeV are compared with the ones in p+p, p+Pb, and Pb+Pb collisions in Fig. 5. The results in Xe+Xe collisions trace the ones from the other collision systems, which exhibits the same behavior as ones reported in Ref. [73].

Figure 6 (a) and (b) show collision energy (in)dependence of hadron yield ratios as functions of multiplicity in nuclear and p+p collisions, respectively. The results in Au+Au collisions at $\sqrt{s_{NN}} = 200$ GeV are compared with the ones in Pb+Pb collisions at $\sqrt{s_{NN}} = 2.76$ TeV in Fig. 6 (a). On the other hand, a comparison in p+p collisions between $\sqrt{s} = 7$ TeV and 100 TeV is made in Fig. 6 (b). It is noted that this extremely large collision energy of $\sqrt{s} = 100$ TeV is the same as the one planned at the Future Circular Collider (FCC) experiment. Tendency is the same as that of the other results again: The hadron yield ratios exhibit scaling behavior as functions of multiplicity and there is almost no collision energy dependence regardless of a gap of collision energy with one or two order of maegnitude for each comparison.

These results demonstrate absence of size and energy dependence for hadron yield ratios as functions of multiplicity. Therefore it can be said that the multiplicity is one of the keys to control the fraction of energy converted into the QGP fluids in high-energy nuclear collisions.

IV. SUMMARY

In this study, we analyzed multiplicity dependence of the hadron yield ratios in various collision systems and in a wide range of collision energy, based on the dynamical core–corona initialization framework, and studied how much in fraction the equilibrated matter is formed in p+p, p+Pb, and Pb+Pb collisions.

Assuming that fluids are generated via four-

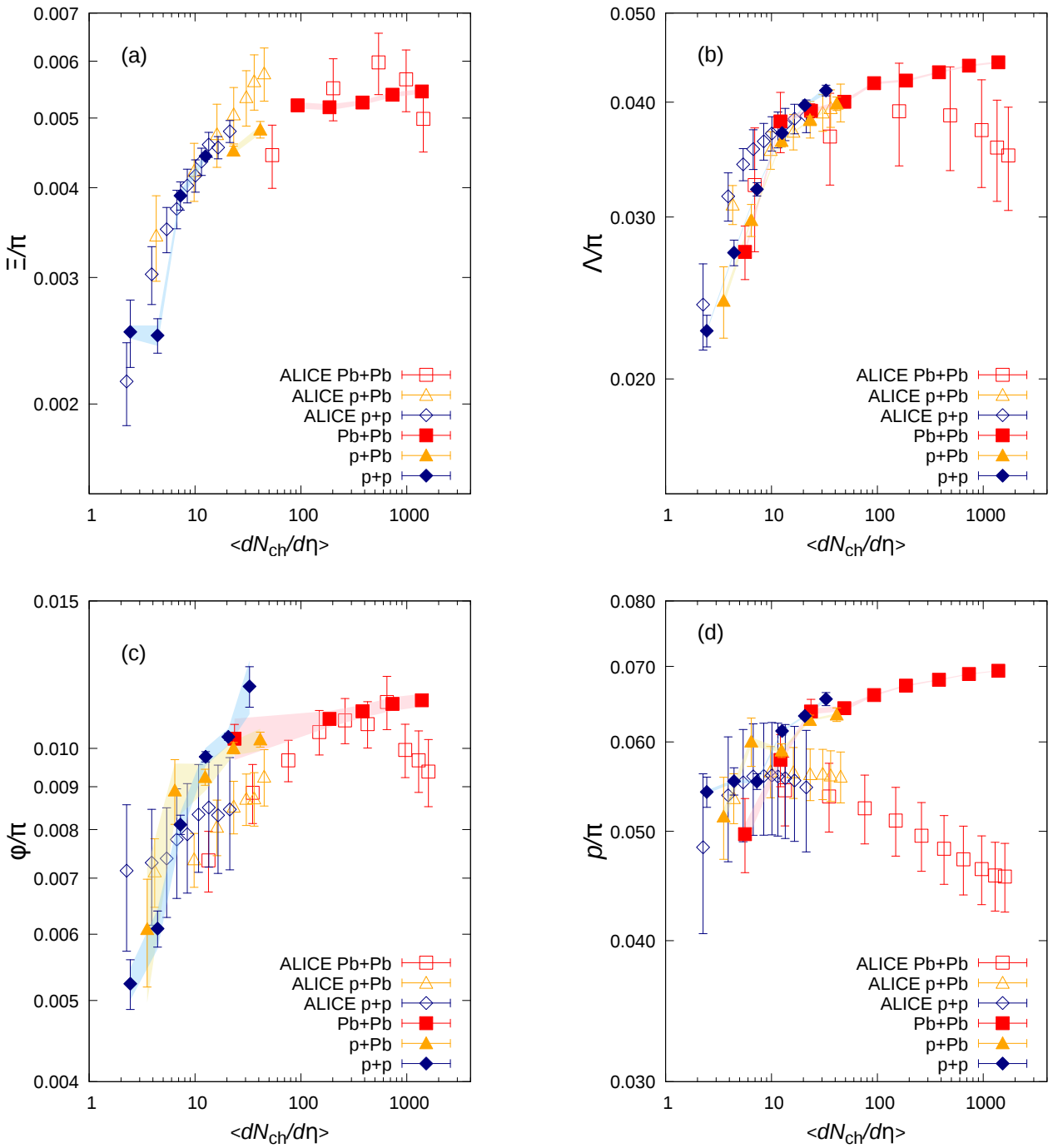

FIG. 4. (Color online) Hadron yield ratios of (a) cascades (Ξ^- and $\bar{\Xi}^+$), (b) lambdas (Λ and $\bar{\Lambda}$), (c) phi mesons (ϕ), and (d) protons (p and $\bar{p}$) to charged pions (π^- and π^+) as functions of multiplicity at mid-rapidity, $\langle dN_{\rm ch}/d\eta\rangle$, in p+p (diamonds), p+Pb (triangles) and Pb+Pb (squares) collisions at the LHC energies. The center-of-mass collision energy per nucleon pair is, $\sqrt{s_{NN}} = 7$ TeV (p+p), 5.02 TeV (p+Pb) and 2.76 TeV (Pb+Pb). Results from the DCCI model (closed symbols) are compared with the ALICE data (open symbols) [37, 65, 67–71].

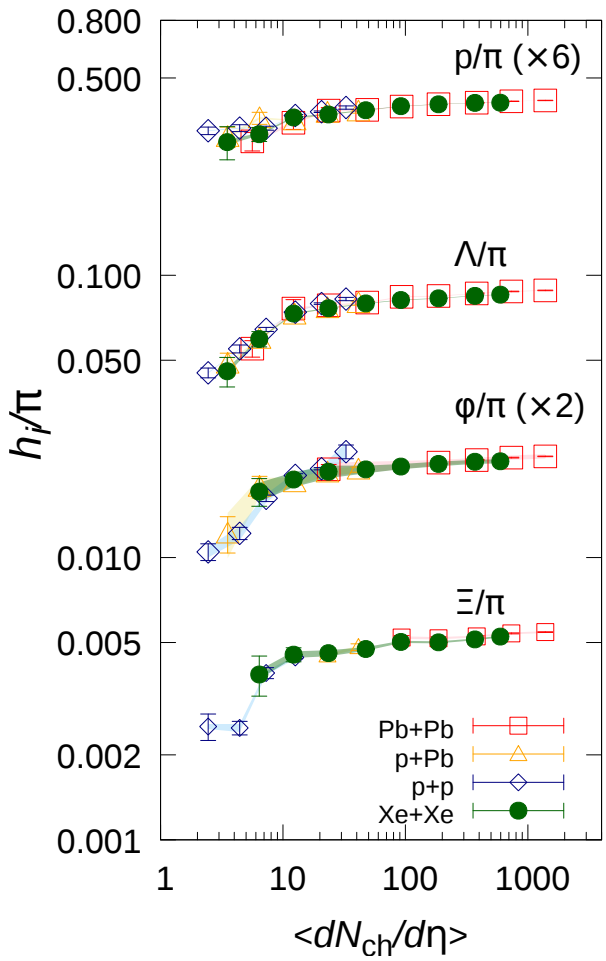

FIG. 5. (Color Online) Hadron yield ratios as functions of multiplicity in Xe+Xe collisions at $\sqrt{s_{NN}} = 5.44$ TeV (closed circles) are compared with the ones in p+p (open diamonds), p+Pb (open triangles), and Pb+Pb (open squares) collisions at LHC energies.

momentum deposition of the initially produced partons, we described the initial stage to form the QGP fluids with hydrodynamic equations with source terms. We formulated the source term considering the spatial geometry of the initial partons under the concept of the core–corona picture. In this picture, partons in high-density region are likely to be components of the QGP fluids, while those in low-density region tend to survive as partons traversing the QGP fluids or vacuum. Using the dynamical core–corona initialization framework, we performed numerical simulations of nucleon–nucleon, nucleon–nucleus, and nucleus–nucleus collisions at RHIC, LHC, and FCC energies. First we generated initial partons with Pythia 8.230 switching off the hadronization. Next we perform the dynamical core–corona initialization from the formation time to the initial time of fluids. QGP fluids are generated through the source term which is expressed as the sum of four-momentum deposition of each parton generated initially. The core and the corona are separated in accordance with density of initial partons based on the core–corona picture. The space-time evolution of QGP fluids (the core) is described by (3+1)-dimensional ideal hydrodynamics. The surviving partons (the corona) keep traversing in the QGP fluids or vacuum. Each system undergoes different hadronization processes. As in a conventional way, we converted the QGP fluids to hadrons via the Cooper–Frye formula at the decoupling temperature. On the other hand, the traversing partons form color singlet strings and are hadronized via string fragmentation with Pythia. Final hadron yields are composed of production of both the core and the corona. Since each hadronization mechanism gives proper value of particle ratios, the ratios in final hadron production reflect the competition between two contributions. As a result of the dynamical core–corona initialization, the fraction of the core increases monotonically with multiplicity, and hadron yield ratios eventually change from the value of the string fragmentation to the one of statistical models.

We analyzed the multiplicity dependence of yield ratios of cascades to charged pions with various values of a_0 which is a parameter to control the fraction of the core in the fluidization rate. Performing chi-square fitting for the yield ratios of our results and the experimental data, we found that $a_0 = 368$ would be the best value to describe the experimental data within our model. Using the extracted a_0, we performed simulations of p+p, p+Pb, and Pb+Pb collisions at LHC energies and quantified the fraction of the fluidized energy at midrapidity. Our result showed that the fraction of fluidized energy increases monotonically with the multiplicity. We concluded that even at the multiplicity in non-single diffractive p+p events there exists hadron production from the chemically equilibrated matter to reproduce monotonically increasing behavior of multiplicity dependence of hadron yield ratios reported by ALICE Collaboration. We also analyzed the multiplicity dependence of yield ratios of cascades, lambdas, phi mesons, and protons with the extracted a_0 in various colliding systems and in a wide range of collision energy. Except for protons, our model calculations showed reasonable agreement with the ALICE experimental data. In the low-multiplicity events $\langle dN_{\rm ch}/d\eta\rangle \approx$ 2-3, hadron yield ratios are almost identical with those from string fragmentation, while in high-multiplicity events with above $\langle dN_{\rm ch}/d\eta\rangle \approx 300$, hadron yield ratios are almost the same as those of statistical models. We described the continuous increase of hadron yield ratios observed in the experimental data as a result of competition between the core and the corona. Although our results describe the experimental data reasonably, we admit that their detailed characteristic is not reproduced. Nevertheless there is still room to introduce additional dynamics such as hadronic rescatterings and viscosity. We leave implementation of them as

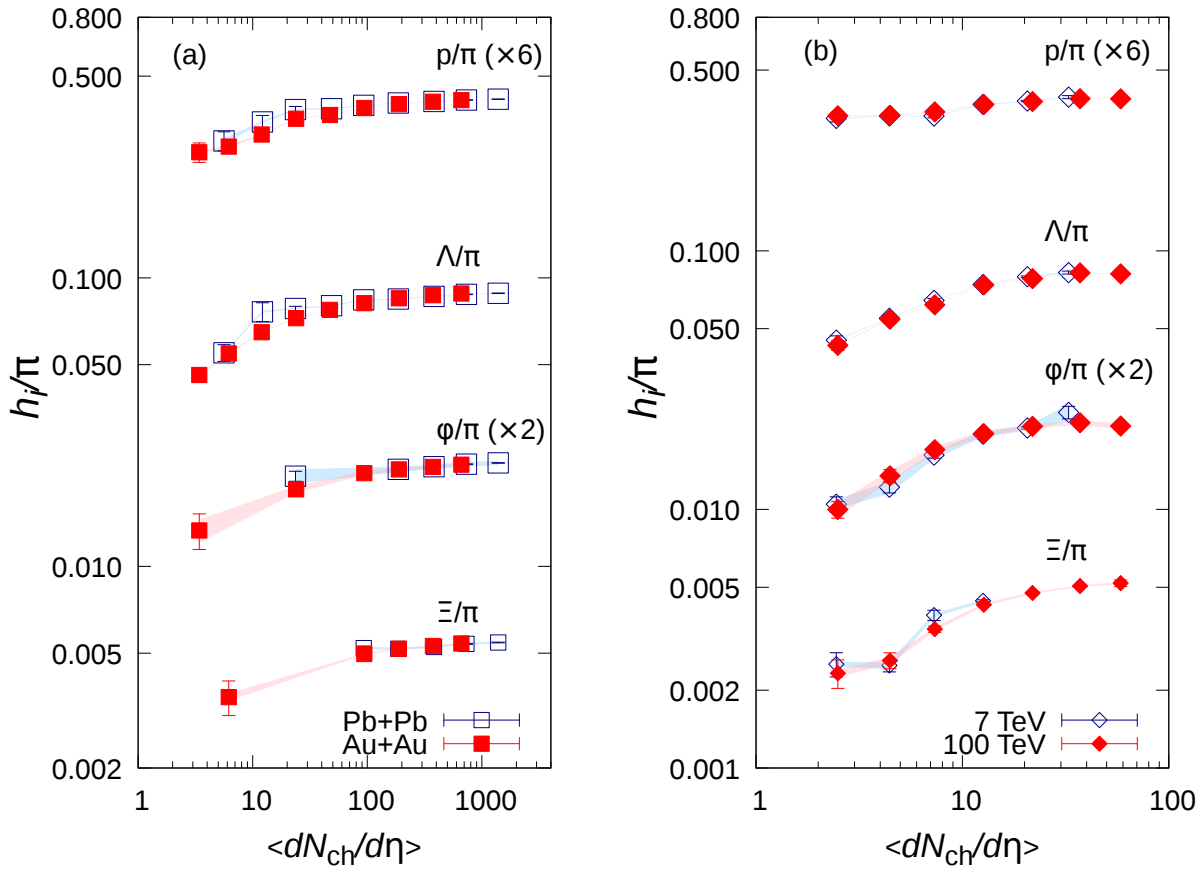

FIG. 6. (Color Online) (a) Hadron yield ratio as a function of multiplicity in heavy-ion collisions at RHIC and LHC energies. Results in Pb+Pb collisions at $\sqrt{s_{NN}} = 2.76$ TeV (open symbols) are compared with the ones in Au+Au collisions at $\sqrt{s_{NN}} = 200$ GeV (closed symbols). (b) Hadron yield ratio as a function of multiplicity in p+p collisions at LHC and FCC energies. Results at $\sqrt{s} = 7$ TeV (open symbols) are compared with the ones at $\sqrt{s} = 100$ TeV (closed symbols).

our future work. In the dynamical core–corona initialization model, system size and collision energy dependences of the hadron yield ratio were analyzed by performing simulations of p+p, Xe+Xe, and Au+Au collisions at $\sqrt{s_{NN}} = 100$ TeV, 5.44 TeV, and 200 GeV, respectively. We studied whether there is the system size dependence of the hadron yield ratio as a function of multiplicity by comparing the results of Xe+Xe collisions with the ones of other collision systems at LHC energies. We also checked whether the collision energy dependence appears comparing results at RHIC energy with the ones at LHC energy, and results in p+p collisions at FCC energy with the ones at LHC energy. Since both results show clear scaling with multiplicity, there are no system size and collision energy dependence within the dynamical core–corona initialization model.

In this work, we focused on the bulk property of the system created in high-energy nuclear collisions and saw that the dynamical core–corona initialization model reasonably describes the multiplicity dependence of strange hadron yield ratios from small to large colliding systems. On the other hand, it is still not revealed to what extent collectivity observed in small colliding systems is originated from the collective hydrodynamic flow of the QGP fluids. Flow observables in small colliding systems have been discussed frequently in the context of QGP formation theoretically and experimentally. We point out here that the bulk properties such as hadron yield ratios also should be explained as well as the flow observables within the same framework. Conventionally viscous hydrodynamic models, which were successful in description of flow observables in high-energy heavy-ion collisions, have been applied also to small colliding systems. However, even if these hydrodynamic models reproduce flow data in small colliding systems, they might not reproduce the bulk properties, in particular, hadron yield ratios. In the light of our analysis and interpretation of hadron yield ratios data, there should exist certain contribution from non-equilibrated systems in the final hadron production which would dilute collective flow signals to some extent. Therefore in our future work we plan to study what extent hydrodynamic flow signals generated by the core

would be affected by the corona as a non-equilibrated system within the dynamical core–corona initialization model. In order to perform sophisticated analysis, we will introduce viscosities in fluids and hadronic re-scatterings in the late stage in the dynamical core–corona initialization model.

It is also worth studying the effect of dynamical core–corona initialization on transverse dynamics in high-energy nuclear collisions. We anticipate high p_T partons behave as the corona and traverse the core after the dynamical core–corona initialization. Thus we separate hard from soft components naturally and dynamically. This would be a starting point to investigate the modification of jet structure in a hydro-based full event generator. These will be discussed in our future publications.

ACKNOWLEDGEMENT

The work by Y.T. is supported in part by a special award from the Office of the Vice President of Research at Wayne State University and in part by the National Science Foundation (NSF) within the framework of the JETSCAPE collaboration under Award No. ACI-1550300. The work by T.H. is partly supported by JSPS KAKENHI Grant Number JP17H02900.

Appendix A: Derivation of fluidization rate

The fluidization rate is obtained by substituting Eq. (6) into the kinetic definition of energy-momentum tensor in Eq. (4). The right hand side of Eq. (4) without minus sign becomes

$$\begin{aligned}
&\partial_\mu T^{\mu\nu}_{\rm parton} \\
&= \sum_i \int d^3p \frac{p^\mu p^\nu}{p^0} \partial_\mu G(\boldsymbol{x}-\boldsymbol{x}_i(t)) \delta^{(3)}(\boldsymbol{p}-\boldsymbol{p}_i(t)) \\
&= \sum_i \int d^3p \frac{p^\mu p^\nu}{p^0} \Big[\big(\partial_\mu G(\boldsymbol{x}-\boldsymbol{x}_i(t))\big) \delta^{(3)}(\boldsymbol{p}-\boldsymbol{p}_i(t)) \\
&\quad + G(\boldsymbol{x}-\boldsymbol{x}_i(t)) \big(\partial_\mu \delta^{(3)}(\boldsymbol{p}-\boldsymbol{p}_i(t))\big) \Big] .
\end{aligned} \tag{A1}$$

The first term in Eq. (A1) vanishes as

$$\begin{aligned}
&\sum_i \int \frac{d^3p}{p^0} p^\nu \left[\left(p^0 \frac{\partial}{\partial t} + \boldsymbol{p}\cdot\nabla \right) \frac{1}{\sqrt{(2\pi\sigma^2)^3}} e^{-\frac{(\boldsymbol{x}-\boldsymbol{x}_i(t))^2}{2\sigma^2}} \right] \\
&\times \delta^{(3)}(\boldsymbol{p}-\boldsymbol{p}_i(t)) \\
&= \sum_i \int \frac{d^3p}{p^0} p^\nu \left[p^0 \frac{\boldsymbol{x}-\boldsymbol{x}_i(t)}{\sigma^2} \cdot \frac{d\boldsymbol{x}_i}{dt} - \boldsymbol{p}_i \cdot \frac{\boldsymbol{x}-\boldsymbol{x}_i(t)}{\sigma^2} \right] \\
&\times \frac{1}{\sqrt{(2\pi\sigma^2)^3}} e^{-\frac{(\boldsymbol{x}-\boldsymbol{x}_i(t))^2}{2\sigma^2}} \delta^{(3)}(\boldsymbol{p}-\boldsymbol{p}_i(t)) \\
&= 0.
\end{aligned}$$

Here we use $p_i^0 d\boldsymbol{x}_i/dt = \boldsymbol{p}_i$. On the other hand, the second term in Eq. (A1) is

$$\begin{aligned}
&\sum_i \int \frac{d^3p}{p^0} p^\nu G(\boldsymbol{x}-\boldsymbol{x}_i)\, p^\mu \partial_\mu \delta^{(3)}(\boldsymbol{p}-\boldsymbol{p}_i(t)) \\
&= \sum_i \int \frac{d^3p}{p^0} p^\nu G(\boldsymbol{x}-\boldsymbol{x}_i)\, p^0 \frac{\partial}{\partial t} \frac{1}{(2\pi)^3} \int d^3x' e^{i(\boldsymbol{p}-\boldsymbol{p}_i(t))\cdot\boldsymbol{x}'} \\
&= -\frac{i}{(2\pi)^3} \sum_i G(\boldsymbol{x}-\boldsymbol{x}_i) \\
&\times \int \frac{d^3p}{p^0} p^\nu p^0 \int d^3x' \frac{d\boldsymbol{p}_i}{dt} \cdot \boldsymbol{x}' e^{i(\boldsymbol{p}-\boldsymbol{p}_i(t))\cdot\boldsymbol{x}'} .
\end{aligned}$$

Finally Eq. (A1) becomes

$$\begin{aligned}
&\partial_\mu T^{\mu\nu}_{\rm parton} \\
&= -\frac{1}{(2\pi)^3} \sum_i G(\boldsymbol{x}-\boldsymbol{x}_i) \\
&\quad \times \int \frac{d^3p}{p^0} p^\nu p^0 \frac{d\boldsymbol{p}_i}{dt} \cdot \frac{\partial}{\partial \boldsymbol{p}} \int d^3x' e^{i(\boldsymbol{p}-\boldsymbol{p}_i)\cdot\boldsymbol{x}'} \\
&= -\sum_i G(\boldsymbol{x}-\boldsymbol{x}_i) \int \frac{d^3p}{p^0} p^\nu p^0 \frac{d\boldsymbol{p}_i}{dt} \cdot \frac{\partial}{\partial \boldsymbol{p}} \delta^{(3)}(\boldsymbol{p}-\boldsymbol{p}_i) \\
&= \sum_i G(\boldsymbol{x}-\boldsymbol{x}_i) \int d^3p \frac{d\boldsymbol{p}_i}{dt} \cdot \frac{\partial p^\nu}{\partial \boldsymbol{p}} \delta^{(3)}(\boldsymbol{p}-\boldsymbol{p}_i) \\
&= \sum_i G(\boldsymbol{x}-\boldsymbol{x}_i) \frac{dp_i^\nu}{dt} .
\end{aligned}$$

Thus the source term (4) is derived as

$$J^\mu(x) = -\sum_i \frac{dp_i^\mu(t)}{dt} G(\boldsymbol{x}-\boldsymbol{x}_i(t)) , \tag{A2}$$

by assuming the phase space distribution as Eq. (6).

Appendix B: Reduced chi-square values of function fitting

Table I shows the reduced chi-square values of function fitting for yield ratios of cascades to pions as functions of

multiplicity with various a_0 parameters shown in Fig. 1. Since the statistical errors from hydrodynamic simulations are relatively small, only the statistical errors due to string fragmentation are considered in the chi-square fitting. We also show the reduced chi-square value from function fitting for the yield ratio of cascades to pions in ALICE experimental data [37].

a_0	collision systems	k	n	reduced χ^2
10	Pb+Pb	577.785	0.656	35.8272
20	Pb+Pb	43.195	0.461	3.61187
50	Pb+Pb	3.03	0.324	2.87592
100	Pb+Pb	4.985	0.459	2.37556
100	p+p, p+Pb, and Pb+Pb	8.595	0.529	11.2227
125	Pb+Pb	6.745	0.68	4.92507
150	Pb+Pb	1.16	0.445	21.4127
1000	Pb+Pb	0.095	0.267	4.87633
N/A	p+p, p+Pb, and Pb+Pb	6.685	1.434	0.971169

TABLE I. Reduced chi-square values in function fittings for yield ratios of cascades to pions as functions of multiplicity for various a_0 parameters in Fig. 1 and for ALICE data [37] at the bottom line.

[1] U. W. Heinz and P. F. Kolb, *Statistical QCD. Proceedings, International Symposium, Bielefeld, Germany, August 26-30, 2001*, Nucl. Phys. **A702**, 269 (2002), arXiv:hep-ph/0111075 [hep-ph].

[2] T. D. Lee, *Quark gluon plasma. New discoveries at RHIC: A case of strongly interacting quark gluon plasma. Proceedings, RBRC Workshop, Brookhaven, Upton, USA, May 14-15, 2004*, Nucl. Phys. **A750**, 1 (2005).

[3] M. Gyulassy and L. McLerran, *Quark gluon plasma. New discoveries at RHIC: A case of strongly interacting quark gluon plasma. Proceedings, RBRC Workshop, Brookhaven, Upton, USA, May 14-15, 2004*, Nucl. Phys. **A750**, 30 (2005), arXiv:nucl-th/0405013 [nucl-th].

[4] E. V. Shuryak, *Quark gluon plasma. New discoveries at RHIC: A case of strongly interacting quark gluon plasma. Proceedings, RBRC Workshop, Brookhaven, Upton, USA, May 14-15, 2004*, Nucl. Phys. **A750**, 64 (2005), arXiv:hep-ph/0405066 [hep-ph].

[5] T. Hirano and M. Gyulassy, Nucl. Phys. **A769**, 71 (2006), arXiv:nucl-th/0506049 [nucl-th].

[6] K. Dusling, W. Li, and B. Schenke, Int. J. Mod. Phys. **E25**, 1630002 (2016), arXiv:1509.07939 [nucl-ex].

[7] J. L. Nagle and W. A. Zajc, Ann. Rev. Nucl. Part. Sci. **68**, 211 (2018), arXiv:1801.03477 [nucl-ex].

[8] S. Chatrchyan *et al.* (CMS), Phys. Lett. **B718**, 795 (2013), arXiv:1210.5482 [nucl-ex].

[9] B. Abelev *et al.* (ALICE), Phys. Lett. **B719**, 29 (2013), arXiv:1212.2001 [nucl-ex].

[10] G. Aad *et al.* (ATLAS), Phys. Lett. **B725**, 60 (2013), arXiv:1303.2084 [hep-ex].

[11] V. Khachatryan *et al.* (CMS), Phys. Rev. Lett. **115**, 012301 (2015), arXiv:1502.05382 [nucl-ex].

[12] A. Adare *et al.* (PHENIX), Phys. Rev. Lett. **111**, 212301 (2013), arXiv:1303.1794 [nucl-ex].

[13] L. Adamczyk *et al.* (STAR), Phys. Lett. **B747**, 265 (2015), arXiv:1502.07652 [nucl-ex].

[14] C. Aidala *et al.* (PHENIX), Nature Phys. **15**, 214 (2019), arXiv:1805.02973 [nucl-ex].

[15] P. Bozek, Phys. Rev. **C85**, 014911 (2012), arXiv:1112.0915 [hep-ph].

[16] A. Bzdak, B. Schenke, P. Tribedy, and R. Venugopalan, Phys. Rev. **C87**, 064906 (2013), arXiv:1304.3403 [nucl-th].

[17] G.-Y. Qin and B. Müller, Phys. Rev. **C89**, 044902 (2014), arXiv:1306.3439 [nucl-th].

[18] K. Werner, M. Bleicher, B. Guiot, I. Karpenko, and T. Pierog, Phys. Rev. Lett. **112**, 232301 (2014), arXiv:1307.4379 [nucl-th].

[19] J. D. Orjuela Koop, R. Belmont, P. Yin, and J. L. Nagle, Phys. Rev. **C93**, 044910 (2016), arXiv:1512.06949 [nucl-th].

[20] M. Habich, G. A. Miller, P. Romatschke, and W. Xiang, Eur. Phys. J. **C76**, 408 (2016), arXiv:1512.05354 [nucl-th].

[21] C. Shen, J.-F. Paquet, G. S. Denicol, S. Jeon, and C. Gale, Phys. Rev. **C95**, 014906 (2017), arXiv:1609.02590 [nucl-th].

[22] W. Zhao, Y. Zhou, H. Xu, W. Deng, and H. Song, Phys. Lett. **B780**, 495 (2018), arXiv:1801.00271 [nucl-th].

[23] A. Dumitru, K. Dusling, F. Gelis, J. Jalilian-Marian, T. Lappi, and R. Venugopalan, Phys. Lett. **B697**, 21 (2011), arXiv:1009.5295 [hep-ph].

[24] K. Dusling and R. Venugopalan, Phys. Rev. Lett. **108**, 262001 (2012), arXiv:1201.2658 [hep-ph].

[25] K. Dusling and R. Venugopalan, Phys. Rev. **D87**, 094034 (2013), arXiv:1302.7018 [hep-ph].
[26] A. Dumitru, L. McLerran, and V. Skokov, Phys. Lett. **B743**, 134 (2015), arXiv:1410.4844 [hep-ph].
[27] B. Schenke, S. Schlichting, and R. Venugopalan, Phys. Lett. **B747**, 76 (2015), arXiv:1502.01331 [hep-ph].
[28] T. Lappi, *Proceedings, 25th International Conference on Ultra-Relativistic Nucleus-Nucleus Collisions (Quark Matter 2015): Kobe, Japan, September 27-October 3, 2015*, Nucl. Phys. **A956**, 537 (2016), arXiv:1512.07209 [hep-ph].
[29] E. Gotsman, E. Levin, U. Maor, and S. Tapia, Phys. Rev. **D93**, 074029 (2016), arXiv:1603.02143 [hep-ph].
[30] B. Schenke, S. Schlichting, P. Tribedy, and R. Venugopalan, Phys. Rev. Lett. **117**, 162301 (2016), arXiv:1607.02496 [hep-ph].
[31] L. McLerran and V. Skokov, Nucl. Phys. **A959**, 83 (2017), arXiv:1611.09870 [hep-ph].
[32] E. Iancu and A. H. Rezaeian, Phys. Rev. **D95**, 094003 (2017), arXiv:1702.03943 [hep-ph].
[33] K. Dusling, M. Mace, and R. Venugopalan, Phys. Rev. Lett. **120**, 042002 (2018), arXiv:1705.00745 [hep-ph].
[34] Y. V. Kovchegov and V. V. Skokov, Phys. Rev. **D97**, 094021 (2018), arXiv:1802.08166 [hep-ph].
[35] M. Mace, V. V. Skokov, P. Tribedy, and R. Venugopalan, Phys. Lett. **B788**, 161 (2019), arXiv:1807.00825 [hep-ph].
[36] C. Zhang, C. Marquet, G.-Y. Qin, S.-Y. Wei, and B.-W. Xiao, Phys. Rev. Lett. **122**, 172302 (2019), arXiv:1901.10320 [hep-ph].
[37] J. Adam *et al.* (ALICE), Nature Phys. **13**, 535 (2017), arXiv:1606.07424 [nucl-ex].
[38] J. Rafelski and B. Muller, Phys. Rev. Lett. **48**, 1066 (1982), [Erratum: Phys. Rev. Lett.56,2334(1986)].
[39] P. Koch, B. Muller, and J. Rafelski, Phys. Rept. **142**, 167 (1986).
[40] A. Andronic, P. Braun-Munzinger, K. Redlich, and J. Stachel, Nature **561**, 321 (2018), arXiv:1710.09425 [nucl-th].
[41] K. Werner, Phys. Rev. Lett. **98**, 152301 (2007), arXiv:0704.1270 [nucl-th].
[42] J. Aichelin and K. Werner, Phys. Rev. **C79**, 064907 (2009), [Erratum: Phys. Rev.C81,029902(2010)], arXiv:0810.4465 [nucl-th].
[43] F. Becattini and J. Manninen, Phys. Lett. **B673**, 19 (2009), arXiv:0811.3766 [nucl-th].
[44] P. Bozek, Acta Phys. Polon. **B36**, 3071 (2005), arXiv:nucl-th/0506037 [nucl-th].
[45] T. Pierog, I. Karpenko, J. M. Katzy, E. Yatsenko, and K. Werner, Phys. Rev. **C92**, 034906 (2015), arXiv:1306.0121 [hep-ph].
[46] K. Werner, A. G. Knospe, C. Markert, B. Guiot, I. Karpenko, T. Pierog, G. Sophys, M. Stefaniak, M. Bleicher, and J. Steinheimer, *Proceedings, 17th International Conference on Strangeness in Quark Matter (SQM 2017): Utrecht, The Netherlands, July 10-15, 2017*, EPJ Web Conf. **17**, 10900 (2018), arXiv:1812.06330 [nucl-th].
[47] M. Okai, K. Kawaguchi, Y. Tachibana, and T. Hirano, Phys. Rev. **C95**, 054914 (2017), arXiv:1702.07541 [nucl-th].
[48] C. Shen and B. Schenke, Phys. Rev. **C97**, 024907 (2018), arXiv:1710.00881 [nucl-th].
[49] Y. Akamatsu, M. Asakawa, T. Hirano, M. Kitazawa, K. Morita, K. Murase, Y. Nara, C. Nonaka, and A. Ohnishi, Phys. Rev. **C98**, 024909 (2018), arXiv:1805.09024 [nucl-th].
[50] Y. Kanakubo, M. Okai, Y. Tachibana, and T. Hirano, PTEP **2018**, 121D01 (2018), arXiv:1806.10329 [nucl-th].
[51] T. Sjostrand, S. Mrenna, and P. Z. Skands, Comput. Phys. Commun. **178**, 852 (2008), arXiv:0710.3820 [hep-ph].
[52] F. Cooper and G. Frye, Phys. Rev. **D10**, 186 (1974).
[53] Y. Tachibana and T. Hirano, Phys. Rev. **C90**, 021902 (2014), arXiv:1402.6469 [nucl-th].
[54] Y. Tachibana and T. Hirano, Phys. Rev. **C93**, 054907 (2016), arXiv:1510.06966 [nucl-th].
[55] Y. Tachibana, N.-B. Chang, and G.-Y. Qin, Phys. Rev. **C95**, 044909 (2017), arXiv:1701.07951 [nucl-th].
[56] W. Chen, S. Cao, T. Luo, L.-G. Pang, and X.-N. Wang, Phys. Lett. **B777**, 86 (2018), arXiv:1704.03648 [nucl-th].
[57] N.-B. Chang, Y. Tachibana, and G.-Y. Qin, Phys. Lett. **B801**, 135181 (2020), arXiv:1906.09562 [nucl-th].
[58] Y. Tachibana, C. Shen, and A. Majumder, (2020), arXiv:2001.08321 [nucl-th].
[59] S. Borsanyi, Z. Fodor, C. Hoelbling, S. D. Katz, S. Krieg, and K. K. Szabo, *Proceedings, 31st International Symposium on Lattice Field Theory (Lattice 2013): Mainz, Germany, July 29-August 3, 2013*, PoS **LATTICE2013**, 155 (2014), arXiv:1312.2193 [hep-lat].
[60] C. Bierlich, G. Gustafson, L. Lönnblad, and A. Tarasov, JHEP **03**, 148 (2015), arXiv:1412.6259 [hep-ph].
[61] C. Bierlich, G. Gustafson, and L. Lönnblad, JHEP **10**, 139 (2016), arXiv:1607.04434 [hep-ph].
[62] C. Bierlich, G. Gustafson, L. Lönnblad, and H. Shah, JHEP **10**, 134 (2018), arXiv:1806.10820 [hep-ph].
[63] A. V. Hill, The Journal of Physiology **40**, i (1910), http://jp.physoc.org/content/40/supplement/i.full.pdf+html.
[64] B. B. Abelev *et al.* (ALICE), Phys. Lett. **B728**, 216 (2014), [Erratum: Phys. Lett.B734,409(2014)], arXiv:1307.5543 [nucl-ex].
[65] J. Adam *et al.* (ALICE), Phys. Lett. **B758**, 389 (2016), arXiv:1512.07227 [nucl-ex].
[66] J. Adam *et al.* (ALICE), Eur. Phys. J. **C77**, 33 (2017), arXiv:1509.07541 [nucl-ex].
[67] B. B. Abelev *et al.* (ALICE), Phys. Rev. **C91**, 024609 (2015), arXiv:1404.0495 [nucl-ex].
[68] J. Adam *et al.* (ALICE), Eur. Phys. J. **C76**, 245 (2016), arXiv:1601.07868 [nucl-ex].
[69] S. Acharya *et al.* (ALICE), Phys. Rev. **C99**, 024906 (2019), arXiv:1807.11321 [nucl-ex].
[70] B. Abelev *et al.* (ALICE), Phys. Rev. **C88**, 044910 (2013), arXiv:1303.0737 [hep-ex].
[71] B. B. Abelev *et al.* (ALICE), Phys. Lett. **B728**, 25 (2014), arXiv:1307.6796 [nucl-ex].
[72] Y. Kanakubo, M. Okai, Y. Tachibana, and T. Hirano, *Proceedings, 8th International Conference on Quarks and Nuclear Physics (QNP2018): Tsukuba, Japan, November 13-17, 2018*, JPS Conf. Proc. **26**, 031021 (2019), arXiv:1901.08189 [nucl-th].
[73] D. S. D. Albuquerque (ALICE), *Proceedings, 27th International Conference on Ultrarelativistic Nucleus-Nucleus Collisions (Quark Matter 2018): Venice, Italy, May 14-19, 2018*, Nucl. Phys. **A982**, 823 (2019), arXiv:1807.08727 [hep-ex].